Global NEST Journal, Vol 26, No 5, 06068

Unveiling the industrial photocatalytic dye degradation of textile effluents using tailored eco-friendly AgO Nanoparticles

Subbulakshmi A.[1] and Sreenivasan V.S.[2]*

[1]Assistant Professor, Department of Mechanical Engineering, PSN College of Engineering and Technology, Melathediyur, Tamil Nadu, India
[2]Associate Professor, Department of Mechanical Engineering, Sri Krishna College of Technology, Coimbatore, Tamil Nadu, India
Received: 16/04/2024, Accepted: 07/05/2024, Available online: 31/05/2024
*to whom all correspondence should be addressed: e-mail: vssreenivasan@ymail.com
https://doi.org/10.30955/gnj.006068

Graphical abstract

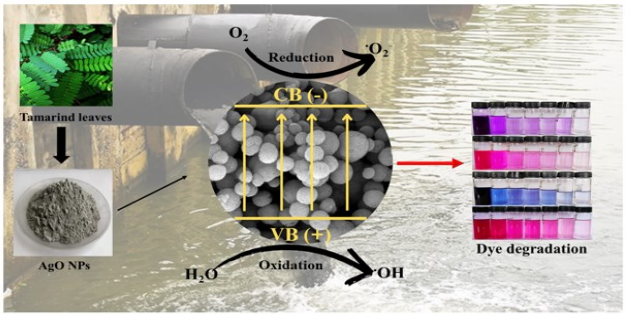

Abstract

In this study, tamarind leaf extract was used to effectively produce silver oxide (AgO) nanoparticles. Crystal violet (CV), Alizarin red (AR), Reactive black (RB), and rhodamine b (Rh B) degradation were examined to evaluate the effectiveness of AgO NPs. XRD patterns, UV-visible spectroscopy, FTIR and SEM analysis were used to analyze the AgO NPs. SEM observations showed spherical morphology size ranging at an average of 58.17 nm. Silver and oxygen were the only elements in the nanostructure, as shown by EDS chemical maps. The synthetic silver nanostructure, with a crystal size of 38 nm, was verified by X-ray diffraction to have the usual cubic structure. The nanostructure showed degradation efficiencies in Crystal violet, Alizarin red, Reactive black, and Rhodamine B, indicating excellent degradation efficiency. All of these results point to the effective production of AgO NPs without the use of any hazardous chemicals, and they point to this material as a potentially beneficial substance for eliminating toxic dye from wastewater made by commercial colouring processes.

Keywords: Textile effluents, dye degradation, tamarind leaves, green synthesis, AgO NPs, photocatalytic activity

1. Introduction

Access to clean water is becoming more and more necessary these days. However, as firms producing paper and ink (Weldegebrieal *et al.* 2020), textiles (Maryam *et al.* 2019), leather, and other materials expand and urbanize, leftover trash from these facilities is being dumped into water bodies, endangering aquatic life as well as human health. The increasing issue of water decontamination from organic contaminants has prompted research into approaches that might provide improved outcomes in wastewater treatment, perhaps lowering the reliance on chemical reagents and minimizing energy use (Tijani *et al.* 2014). An effective approach involves the oxidation of the contaminants, perhaps leading to their total mineralization. Industrial pollutants pose a major threat to the environment because which are very persistent chemically and difficult to decompose. As a result, finding effective ways to remove these colours from wastewater requires scientific research. The most common pollutants in water are Azo dyes. In the textile industry, they are primarily used as colourants. While most of them possess better fixation capabilities, a significant percentage of the dyes between 10 and 15% and as much as 50%, in the case of reactive dyes—could not be accepted by the fabrics during colouring and discharge as a waste stream. Before wastewater-containing factories, dyes are released into the environment, they must be treated because even very fewer concentrations of dye (< 1 ppm) (Abu *et al.* 2022). Several established techniques, including chemical oxidation (Ahmed *et al.* 2021), reduction (Saravanan *et al.* 2021), adsorption (Patel *et al.* 2022), precipitation (Ang *et al.* 2020), coagulation (Zhao *et al.* 2021), flocculation (El-Gaayda *et al.* 2021), flotation (Saleh *et al.* 2022), etc., are already in use to treat wastes. However, the issue with these techniques is that they either generate a lot of sludge during treatment, which makes them typically inefficient, or they only partly break down the dyes, producing additional hazardous metabolites. Among the advanced oxidation processes, silver oxide photocatalysis is one of the most promising. The use of nanomaterials in solving material science problems is growing in importance. The AgO NPs are among the several types of metal nanoparticles that have been investigated extensively due to their strong conductivity, excellent absorption of light, high sensitivity, antibacterial activity, resolution, and chemical stability (Pryshchepa *et al.* 2020). Making AgO NPs at the nanoscale is one of the most exciting areas in nanotechnology. In the medicinal field, AgO NPs have been

used in multiple treatments such as cancer, diabetes, malaria, HIV, and tuberculosis. However, a highly dependable, affordable, and environmentally friendly green synthesis process was made possible by the high production costs and toxicity difficulties associated with the aforementioned methodologies. Applications for silver nanoparticles are many and include food processing, cosmetics, household cleaning, catalysis, clothing manufacturing, and medical applications. The AgO nanoparticles' appealing physicochemical characteristics have got a lot of concern (Garg *et al.* 2022).

The edible fruit of the leguminous Tamarindus indica tree is native to tropical Africa and has spread to Asia. Tamarindus is the single species in the genus, which makes it monotypic. It belongs to the family Fabaceae. There are many applications for tamarind, including food for humans, medicine, and animal feed. Indian reports date back to when tamarind was originally used medicinally. Traditional African and Indian remedies have made substantial use of the leaves, fruits, and seeds of the tamarind plant. Tamarind leaves are used to cure multiple conditions, including liver problems, intestinal worms, fever, coughs, and throat infections when combined with salt and water (Devi *et al.* 2020). In the liver, leaf extracts also show antioxidant action. Young leaves are said to treat cuts, sprains, and various eye diseases. The leaves and fruit extracts of Tamarindus indica were subjected to phytochemical analysis, which revealed the presence of phenols, tannin, saponin, flavonoids, reducing sugar, and anthraquinone. AgO NPs are created when these different phytochemicals are present (Borquaye *et al.* 2020). In the current study, the AgO NPs have been prepared by tamarind leaf extract and various dyes were used in degradation under sunlight using UV-visible spectroscopy. These dyes are considered the harmful and most toxic colourants. The degradation of dyes with colour changes and kinetics has been mentioned.

2. Experimental procedure

2.1. Materials required

The Silver nitrate ($AgNO_3$), Tamarind leaves, Ethanol (99%), AR, CV, RB, and Rh B are the solvent and initial components used to make AgO NPs. Analytical grade reagents (AR) included all of the chemicals, which were procured from Merck in India and were utilized deprived of supplementary cleansing.

2.2. Green extract formulation

In the Indian state of Tamil Nadu, tamarind leaf harvesting is a popular activity. The tamarind leaves were first air-dried in a shaded area for a little, then thoroughly cleaned with distilled water to eliminate any remaining contaminants, and then allowed to dry entirely. The dried leaves are ground into a powder using a regular kitchen mixer to create the extract. Before heating the powdered leaves to 100ºC, 100 ml of hot distilled water was added to make the extract. After incubating for one day, a continuous string and leaf extract were seen. Afterwards, filter paper was used to separate the extracted material for further usage (Borquaye *et al.* 2020).

2.3. Synthesis of AgO NPs

After 30 minutes of defrosting in a 60°C whisking bath, dissolve about 0.1 M of $AgNO_3$ in 90 ml of distilled water. Step two involves combining the silver nitrate solution with the extract mentioned before, using 10 ml. Keep stirring the mixture at 300 rpm until it reaches a yellowish-brownish hue. At that point, the presence of AgO NPs was confirmed by the noticeable shift in the solution's hue from yellow-brown to dark brown. Figure 1 displays the results of the UV-vis spectroscopy, which were used to verify the formation of the silver oxide nanoparticles. In order to collect and dry the precipitate for further analysis, the solution was filtered and then centrifuged for 20 mins at 10,000 rpm.

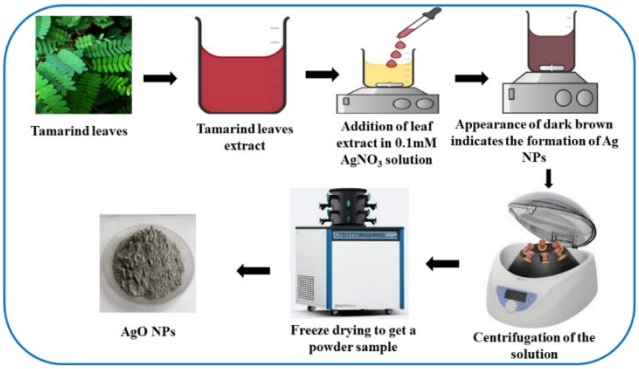

Figure 1. Synthesis of silver oxide nanoparticles

2.4. Preparation of dyes for photocatalytic degradation

The photocatalytic dilapidation of dyes in the presence of AgO NPs under sunlight was analysed as follows. In simple terms, 100 ml of aqueous dyes were mixed with 100 mg of produced AgO NPs individually (100 mg/L). An adequate volume of the dye solution supernatant was exposed to a UV-vis spectrophotometer examination every fifteen minutes throughout the 90 min exposure period of nanoparticle-suspended dyes in the sun. The UV-visible spectra were then regularly recorded, and the degree of dye decolorization was assessed concerning their optical absorption. Moreover, dye degradation efficiency of AgO NPs in the presence of sunlight (Naren *et al.* 2024) estimated where the final and initial concentrations are denoted by C_t and C_0 of AR, CV, RB, and Rh B dyes.

$$\text{Dye degradation efficiency } \eta = \left(1 - \frac{Ct}{C0}\right) \times 100\ \% \quad (1)$$

2.5. Characterization techniques

To analyse the structural properties of produced AgO NPs, a powder XRD was used, molecular vibration and functional groups were chronicled in the 400–4000 cm^{-1} range by FTIR spectroscopy (PerkinElmer, USA). KBr was blended with a powder sample in a ratio of 200:1 and then an identical pellet was prepared, KBr served as a dynamic medium for the Infrared source. The mean size distribution was calculated using DLS concept. The morphology and surface topography of AgO NPS were analyzed using FESEM with EDX for the identification of elemental composition in the material. The luminescence characteristics of the produced AgO NPs were investigated using photoluminescence spectroscopy (Cary Eclipse, Singapore).

3. Results and discussion

The Figure 2 displays a prominent X-ray diffraction peak, with measured 2θ values of 38.13 and 44.31, 64.46, 77.41, and 81.55 that match to (111), (200), (220), (311), and (222) planes of AgO NPs, correspondingly which are compatible with standard JCPDS No. 04-0783 and fit the FCC structure of AgO. The presence of sharp peaks of only silver oxide nanoparticles indicates the high purity and crystalline nature of the prepared material. This indicates that tamarind leaves have played a decisive part in the creation of the crystalline structure of the AgO NPs. The Crystallite size of AgO NPs is found by the Equation 2 (Riaz *et al.* 2022),

$$D = \frac{K\lambda}{\beta\cos\theta} \quad (2)$$

Where, D represents the typical crystallite size, K denotes the form factor (0.9), 1.541 indicates the wavelength of Cu radiation, the fill width half maximum (FWHM) of reflection situated at 2θ, and the angle of reflection in degrees. These variables were utilized to establish a relationship between the crystallite size and the line broadening. The AgO nanoparticles have been measured to have an average crystal size of 38 nm.

The number of dislocation lines per unit crystal volume is referred to as the dislocation density and may be computed using the Williamson–Smallman relation, which can also be estimated (Riaz *et al.* 2022).

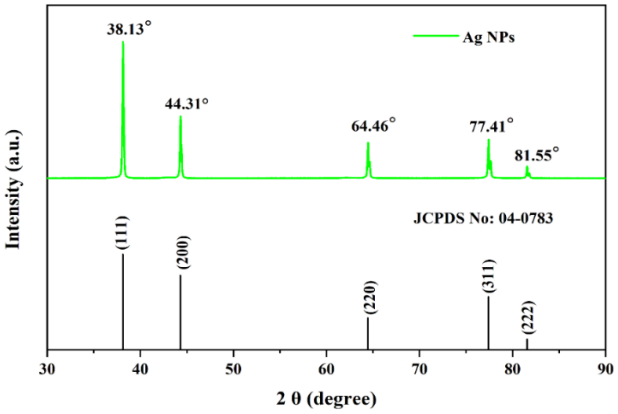

Figure 2. XRD analysis of AgO NPs

$$\text{Dislocation density} = 1/D^2 \quad (3)$$

There is a chance that a tiny strain in the crystal lattice may affect the X-ray diffraction lines' growth. It is possible to Figure out by using the formula (Riaz *et al.* 2022).

$$\varepsilon = \frac{\beta}{4\tan\theta} \quad (4)$$

Where, β is the broadening of the line at FWHM in radians, half of the 2θ, microstrain in radians (i.e., the ratio of peak width to peak location), and ε is the Braggs angle in degrees.

Table 1. The findings from XRD analysis and Rietveld's refinement

Crystal structure	**:**	**Cubic**
Space group	:	Fm3m
Crystal size	:	38 nm
Space group number	:	225
Lattice parameter	:	4.0860 (a=b=c)
Volume	:	68.217 Å
Lattice strain	:	0.0024
Micro strain	:	0.28 %
Dislocation density	:	0.69×10^{-3} $(nm)^{-2}$
R_p	:	3.4328
R_{wp}	:	4.0814
R_{ex}	:	4.0118
Chi^2	:	1.94

The Rietveld refinement for the Tamarind leaves prepared AgO NPs is given in Figure 3. This change aims to highlight the disparities between the observed and anticipated XRD data patterns. Full prof analytical software uses the pseudo-Voigt profile function to refine the Rietveld refinement. Table 1 shows the optimized parameters and the obtained R factors.

The size and morphology of AgO NPs were analyzed using FESEM which are depicted in Figure 4. Before taking FESEM pictures, an aqueous solution of AgO NPs was allowed to settle on a thin layer of quartz. The observed wide size diversity of AgO NPs was consistent with the spherical shape in an agglomerated state as shown by the dynamic light scattering approach and observed absorption. The agglomeration of each nanoparticle indicated a high surface charge (Selmani *et al.* 2020). Additional EDX examination demonstrates that only oxygen and silver are present, which accounts for the material's excellent purity. Hence, the phytochemicals of Tamarind leaves extract caps over the nanoparticle and tune the morphology into a sphere.

The particle size and distribution capability of AgO NPs are depicted in Figure 5. Using the DLS technique, the typical particle size (d50) of AgO NPs is displayed to be 58.17 nm. The broad peak indicates the presence of almost similar particle sizes of all nanoparticles (Salayova *et al.* 2021). The observed particle size agrees with the previously obtained XRD crystal size and SEM images. Hence the Tamarind leaf extract has foremost part in the reduction of particle size in the nano range. The Figure 6 displays the FTIR spectrum of AgO NPs. The maxima in the identified functional groupings are located at 3428 cm^{-1} and 2923 cm^{-1}, 2852 cm^{-1}, 2395

cm^{-1}, 1763 cm^{-1}, 1642 cm^{-1}, 1382 cm^{-1}, 824 cm^{-1}, and 465 cm^{-1}. Stretching of the hydrogen, amino, and alcohol groups is the cause of the prominent FTIR sign at 3428 cm^{-1} (Ibrahim *et al.* 2020). The presence of the alkanes group is shown by the asymmetrical and symmetrical bending of $=CH_2$ and $-CH_3$ sets, which accounts for the high peak at 2923 cm^{-1} and 2852 cm^{-1} (Pirot *et al.* 2023). A band at 2395 cm^{-1} as a consequence of the reaction of the extract with $AgNO_3$. The C=O stretching of ketones is shown by the absorption band at 1763 cm^{-1}. The stretching vibrations of the C=C (aliphatic) rings are responsible for the peaks at 1642 cm^{-1}. The N=O stretching vibration of the nitro groups in leaf extract is best seen by the band at 1382 cm^{-1} (Sun *et al.* 2021).

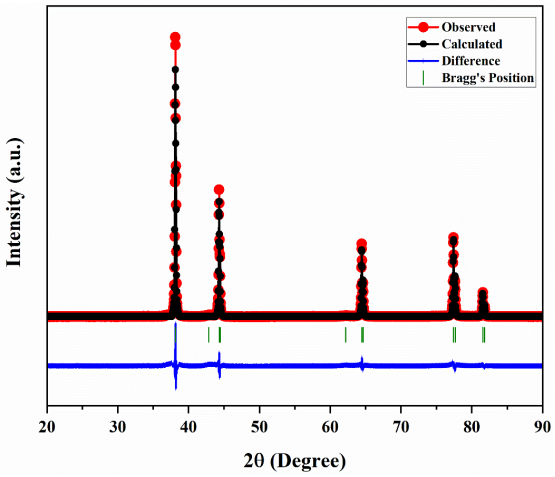

Figure 3. Rietveld's refinement for XRD of AgO NPs

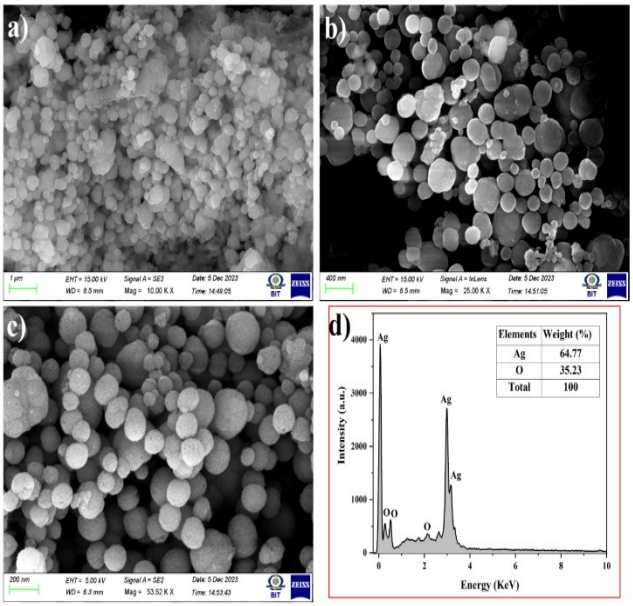

Figure 4. Morphology and primary composition of AgO NPs

The appearance of these functional groups suggests that phytochemicals and silver nanoparticles are related. The peak at 824 is characteristic of an aromatic ring. The AgO metal formation is the cause of the band seen at 465 cm^{-1} (Joseph *et al.* 2015). According to the FTIR results, the functional attachments in the leaf extract, such as OH, NH, and N=O, are most likely what causes Ag^+ ions to change into metallic silver nanoparticles. These same functional groups also serve as the main capping agent that contributes to the increased stability of the synthesized AgO NPs and prevents the nanoparticles from clumping together in the medium.

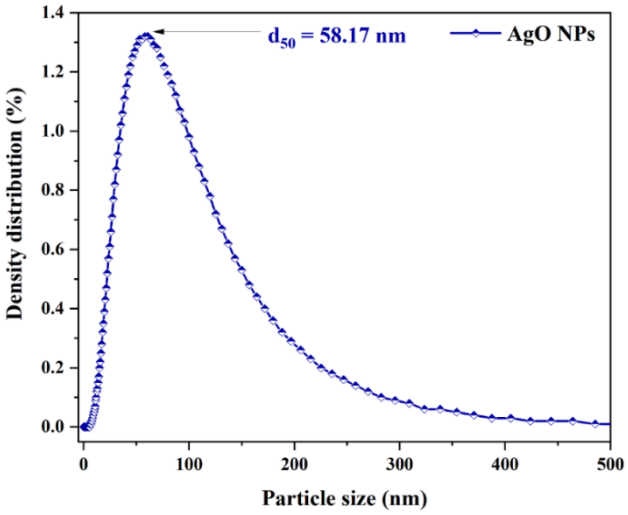

Figure 5. Particle size analysis of AgO NPs

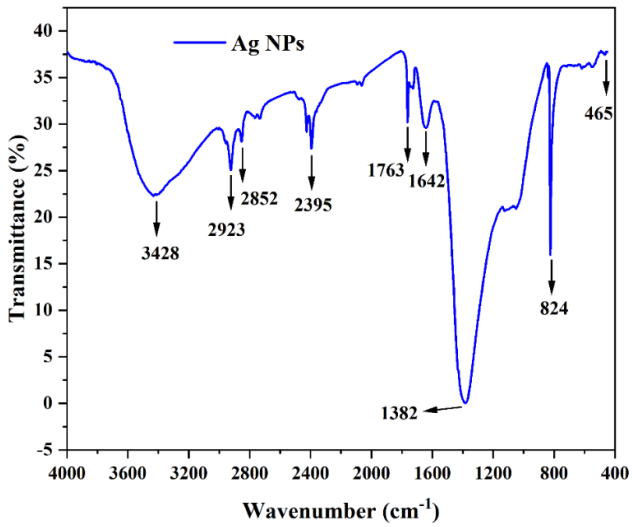

Figure 6. FTIR spectra for AgO NPs

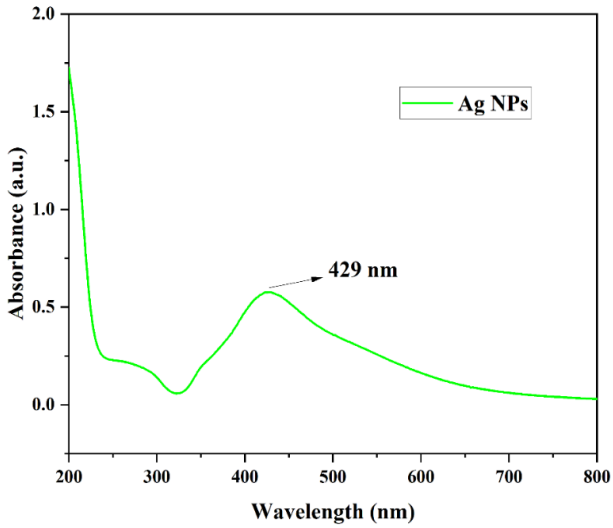

Figure 7. UV-visible spectra of AgO NPs

The Figure 7 displays the optical properties of the AgO NPs that were synthesized. Surface plasmon resonance roots the decrease of silver (Ag^+) into silver NPs, which have a dark yellowish-brown color. The strong band may be seen between 380 nm and 450 nm, where a prominent, distinctive peak absorbs at 429 nm.

This suggests that the produced colloidal solution is optically active, and the substance may be AgO NPs. Based on the UV-Vis spectrum data, it can be inferred that the aqueous solution of $AgNO_3$ and the extract of tamarind leaves reacted to effectively manufacture AgO NPs. The absorption spectra of AgO NPs were used to determine the direct bandgap using Tauc's plot. Using the formula, the absorption efficiency and incident photon energy are connected (Uddin *et al.* 2020).

$$\alpha(\upsilon)h = K(hv - Eg)^n \quad (5)$$

The intended band gap of the prepared AgO is 2.68 eV shown in Figure 8. Between the bottom of the conduction band and the top of valence band, the bandgap is the region with the least energy difference.

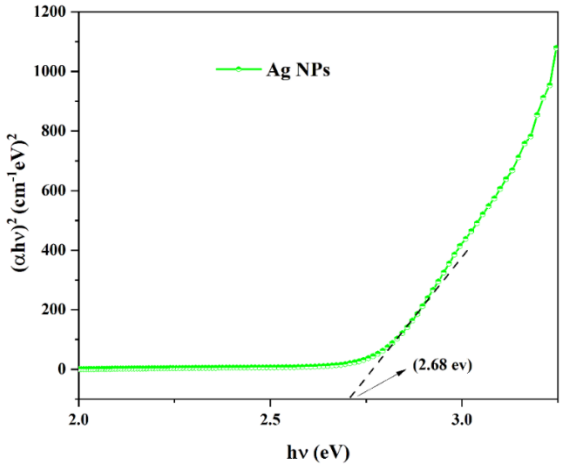

Figure 8. Calculated bandgap for prepared AgO NPs

One theory for the photoluminescence of noble metals is that it results from the innervation of e^- from filled d bands into statuses that are higher than fermi. Following energy loss and subsequent processes of electron-phonon scattering, photoluminescence was produced by the reaction of an electron from a drenched sp band with the hole. The room temperature luminescence spectrum of AgO NPs is shown in Figure 9. It has an emission wavelength of 579 nm and a high excitation peak of 429 nm. A stronger red shift was seen in the emission peak in the direction of the higher wavelength. The excellent purity of the produced AgO NPs is shown by the single strong peak. The steep peak shows where the material transitions from band to band (Woo *et al.* 2023). The presence of a single peak indicates the monocrystalline nature of the material.

The photocatalytic degradation activity of AgO NPs synthesized using Tamarind leaves extract is evaluated by analyzing the photocatalytic activity of various dyes under sunlight irradiation for 90 mins. With increasing time, the absorption peaks' strength steadily drops in the presence of sunlight without affecting the peaks' location. Additionally, the absorbance of dye degradation increases with concentration. The degradation efficiency, rate, and decolorization of various dyes are shown in Figure (10,11,12,13)Af. Even though the results clearly show that the dye's initial rate of degradation was modest, it gradually increased as the exposure period was extended. The various dyes used for the degradation are CV, AR, Rh B, and RB which are a combination of anionic and cationic dyes. Among the dyes, CV shows the highest degradation efficiency of 99 % within 90 minutes. The experiment is also conducted without the presence of sunlight (dark condition) and a catalyst. The results imply the importance of the presence of both catalyst and sunlight.

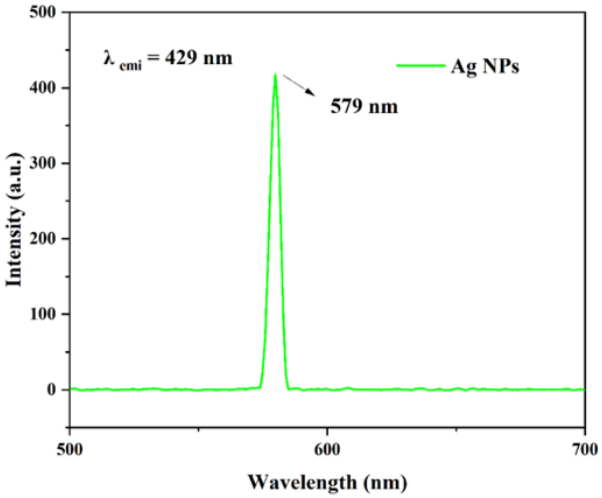

Figure 9. Photoluminescence spectra of AgO NPs

One important finding in the UV-visible examination of the photocatalysis of AR, CV, Rh B, and RB was that the photochemical process required 90 minutes of exposure to sunlight. Based on the experiment, a mechanism of dye photocatalytic activity after AgO NPs were exposed to radiation proposes that an electron is ejected from VB to CB (e^-_{cb}) and h^+_{vb} is formed. It is a strong Lewis acid that prevents recombination with holes in the VB due to the half-filled d-orbitals in the CB having well-trapped electrons (Li *et al.* 2021). Ag^+ ions with four electrons become less common, which finally leads to instability. This facilitates the production of $O_2^{\cdot -}$ by allowing the electron in CB to be imprisoned again and occupied by O_2 molecules, which are then transformed into active OH^- ions (Jeon *et al.* 2021). The phases in the decolorization process of AgO NPs are as follows:

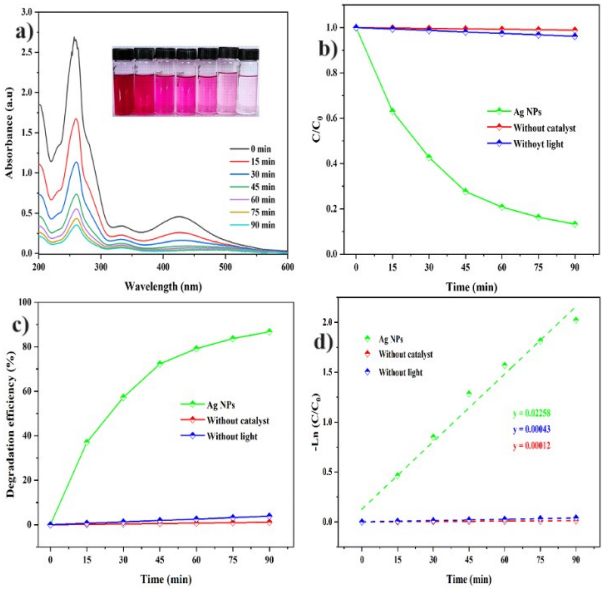

Figure 10. Photocatalytic activity of AgO NPs against Alizarin Red a). Degradation graph, b). C/C0, c). Degradation efficiency, d). Kinetics

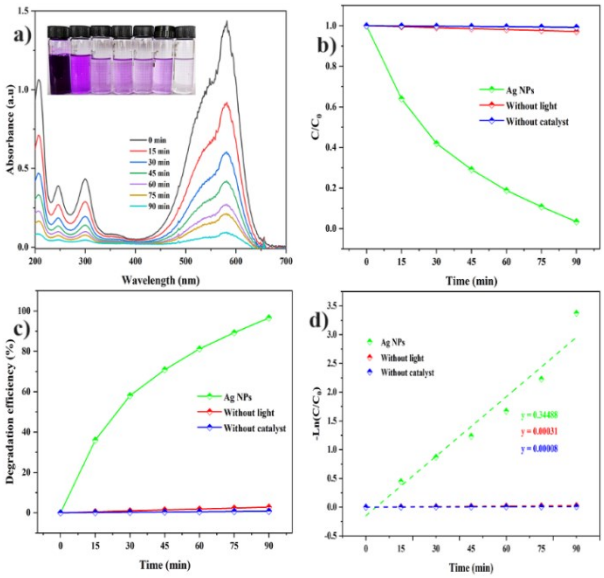

Figure 11. Photocatalytic activity of AgO NPs against Crystal violet a). Degradation graph, b). C/C0, c). Efficiency, d). Kinetics

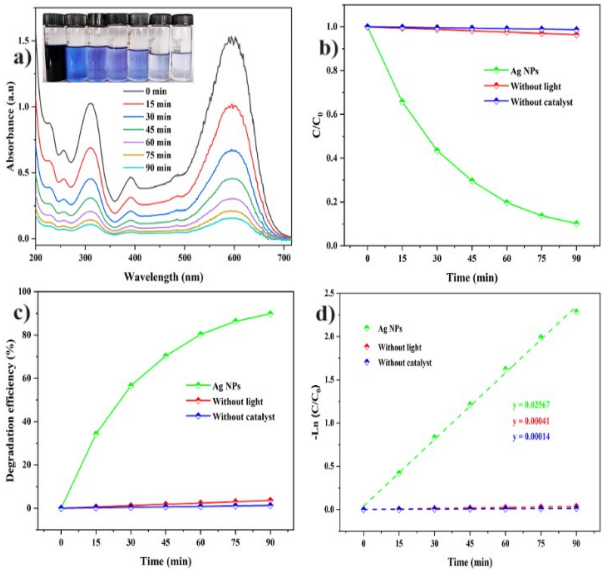

Figure 12. Photocatalytic activity of AgO NPs against Reactive black a). Degradation graph, b). C/C0, c). Efficiency, d). Kinetics

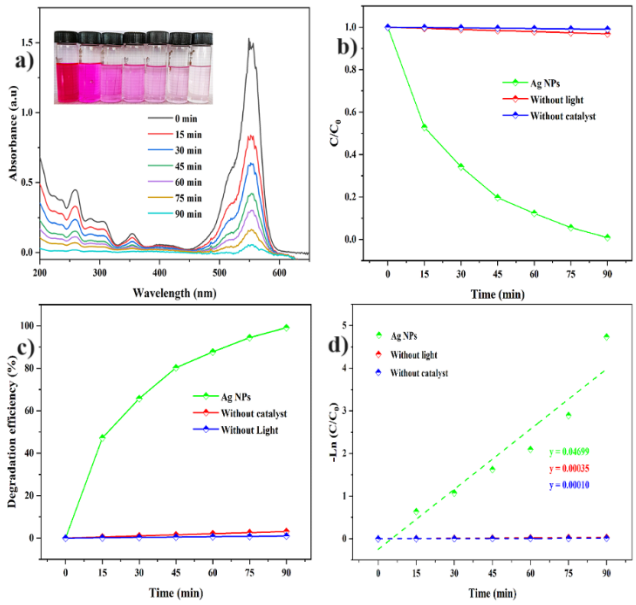

Figure 13. Photocatalytic activity of AgO NPs against Rhodamine B a). Degradation graph, b). C/C0, c). Efficiency, d). Kinetics

$$AgO + hv \rightarrow Ag\left(e^-_{cb} + h^+_{vb}\right) \quad (6)$$

$$Ag + + \left(e^-_{cb}\right) \rightarrow Ag^0\,(\text{Trapping}) \quad (7)$$

$$Ag^0 + O_2 \rightarrow Ag^+ + O_2^{*-}\,(\text{Transfer}) \quad (8)$$

$$O_2^{*-} + H^+ \rightarrow {}^*OOH \quad (9)$$

$${}^*OOH + H^+ + e^-_{cb} \rightarrow H_2O_2 \quad (10)$$

$$H_2O_2 + e^-_{cb} \rightarrow {}^*OH + OH^- \quad (11)$$

However, the generation h^+_{vb} by light may be caught on the catalyst's surface and transfer its control to the OH^- ions or H_2O adsorbed on the upper layer to create dynamic OH* types (Ramaswamy *et al.* 2011), as seen below:

$$h^+_{vb} + H_2O \rightarrow H^+ + {}^*OH$$

$$h^+_{vb} + OH^- \rightarrow {}^*OH$$

Thus, charge carriers formed as a result of the AgO NPs. The high production of hydroxyl ions subsequently results in the decolorization of different dyes, and Figure 14 illustrates the suggested mechanism of photocatalytic activity.

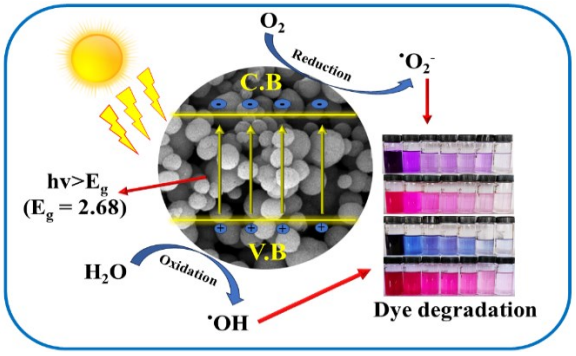

Figure 14. Photocatalytic mechanism of AgO NPs

The kinetics for AR, CV, Rh B, and RB are depicted in Figure(10, 11, 12, 13 – d) which illustrates the Langmuir-Hinshelwood model and uses the following equation to determine the rate of degradation constant (Ramaswamy *et al.* 2011).

$$r = -\frac{dC}{dt} = \frac{kKC}{1+KC}$$

Where, the variables r, C, t, and K represent the speed of degradation of dye (mg/min), dye concentration (mg/l), dye absorption coefficient (l/mg), and rate constant (mg/min), respectively. Since C might be smaller in a diluted solution, it is insignificant, therefore the equation can be expressed as,

$$ln\frac{C}{C0} = kKt$$

Figure (10, 11, 12,13 – d) displays the first-order kinetics of the dyes' photo-degradation process, including AR, CV, Rh B, and RB. Plotting C/C_0 vs. time shows variations in the concentrations of AR, CV, Rh B, and RB suspended with AgO NPs. The first-order rate of dilapidation constant may be found by calculating the slope of a straight line on a plot of -In (C/C_0) versus time. For AR, CV, Rh B, and RB, the degradation constant is 0.0225, 0.0344, 0.04699, and 0.02567 min^{-1}, in that order. Similarly, the rate of degradation without a catalyst is 0.00043, 0.00008, 0.00019, and 0.00014 min^{-1} for AR, CV, Rh B, and RB, respectively. Likewise, the degradation constant under dark conditions under the presence of a catalyst is 0.00012, 0.00031, 0.00035, and 0.00041 min^{-1} for AR, CV, Rh B, and RB respectively. Hence, it indicates the importance of the presence of light and catalyst in the dye solution.

The AgO NPs' stability and recyclable nature have been shown for every dye shown in Figure 15, making them a crucial criterion for photocatalytic applications. Under direct sunlight, the recycling cycles for the photocatalytic degradation of all colours on AgO NPs were completed. The NPs' recyclability may be achieved by gathering them after the photocatalytic process, washing them several times in

water and ethanol using a centrifuge, drying them in a hot air oven, and then utilizing them for the subsequent cycle. It is evident that after five consecutive cycles, the dyes reach their degradation percentages of 83.17, 91.84, 84.67, and 94.74% for AR, CV, RB, and Rh B, correspondingly. This suggests that AgO NPs have outstanding dye degradation photocatalytic stability and recyclability.

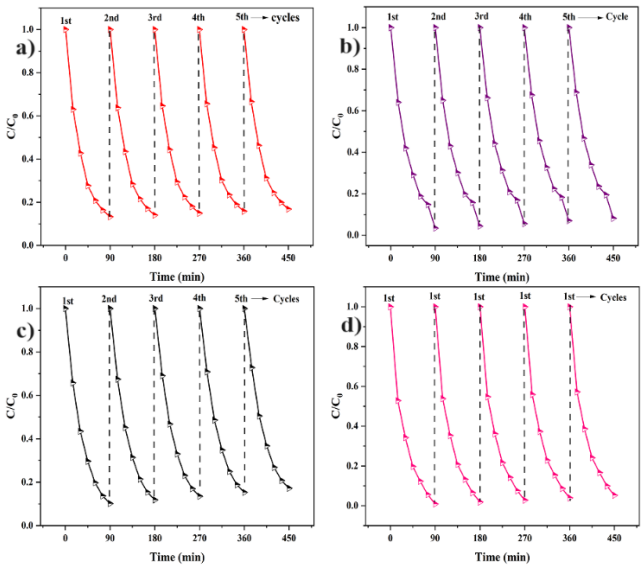

Figure 15. Recyclability of AgO NPs over AR (a), CV (b), RB (c), and Rh B (d) dyes

4. Conclusion

Tamarind leaf extract was used to create AgO NPs in an economical and environmentally friendly way. Studies were also conducted on the role that light and catalysts play in the dye degradation process. The maximum decolourisation occurs at AR, CV, RB, and Rh B are 86, 96, 89, and 99 % respectively within 90 mins which has a degradation rate of 0.0225, 0.0344, 0.04699, and 0.02567 min^{-1} respectively. Thus, dye degradation with eco-friendly AgO NPs is highly beneficial for industrial dye degradation applications.

References

Abu N.S.M., Shah S.S. and Chaity S.B. (2022). Jute stick extract assisted hydrothermal synthesis of zinc oxide nanoflakes and their enhanced photocatalytic and antibacterial efficacy, *Arabian Journal of Chemistry*, **15**, 104265.

Ahmed S.F., Mofijur M. and Nuzhat S. (2021). Recent developments in physical, biological, chemical, and hybrid treatment techniques for removing emerging contaminants from wastewater, *Journal of Hazardous Materials*, **416**, 125912.

Ang W.L. and Mohammad A.W. (2020). State of the art and sustainability of natural coagulants in water and wastewater treatment, *Journal of Cleaner Production*, **262**, 121267.

Borquaye L.S., Doetse M.S., Baah S.O. and Mensah J.A. (2020). Anti-inflammatory and anti-oxidant activities of ethanolic extracts of Tamarindus indica L. (Fabaceae), *Cogent Chemistry*, **6**, 1743403.

Devi B. and Boruah T. (2020). Tamarind (Tamarindus indica). In: Nayik GA, Gull A (eds) Antioxidants in Fruits: Properties and Health Benefits. *Antioxidants in Fruits: Properties and Health Benefits*, **1**, 317–332.

El-Gaayda, J., Titchou, F.E. and Oukhrib, R. (2021). Natural flocculants for the treatment of wastewaters containing dyes or heavy metals: A state-of-the-art review, *Journal of Environmental Chemical Engineering*, **9**, 106060.

Garg, R., Rani, P. and Garg, R. (2022). Biomedical and catalytic applications of agri-based biosynthesized silver nanoparticles, *Environmental Pollution*, **310**, 119830.

Ibrahim, H.M., Reda, MM. and Klingner, A. (2020). Preparation and characterization of green carboxymethylchitosan (CMCS) - Polyvinyl alcohol (PVA) electrospun nanofibers containing gold nanoparticles (AuNPs) and its potential use as biomaterials, *International Journal of Biological Macromolecules*, **151**, 821–829.

Jeon J., Eom K. and Hong Y. (2021). Hot Electron Tunneling in $Pt/LaAlO_3/SrTiO_3$ Heterostructures for Enhanced Photodetection, *ACS Applied Mater Interfaces*, **13**, 47208–47217.

Joseph S. and Mathew B. (2015). Microwave-assisted green synthesis of silver nanoparticles and the study on catalytic activity in the degradation of dyes, *Journal of Molecular Liquids*, **204**, 184–191.

Li S., Wang J. and Xia Y. (2021). Boosted electron-transfer by coupling Ag and Z-scheme heterostructures in CdSe-Ag-WO_3-Ag for excellent photocatalytic H_2 evolution with simultaneous degradation, *Chemical Engineering Journal*, **417**, 129298.

Maryam B. and Büyükgüngör H. (2019). Wastewater reclamation and reuse trends in Turkey: Opportunities and challenges, *Journal of Water Process Engineering*, **30**, 100501.

Naren V.T.M., Surendhiran S. and Jagan K.S.G. (2024). Surface chemistry of phytochemical enriched MgO nanoparticles for antibacterial, antioxidant, and textile dye degradation applications, *Journal of Photochemistry and Photobiology A: Chemistry*, **448**, 115349.

Patel A.K., Singhania R.R. and Albarico F.P.J.B. (2022). Organic wastes bioremediation and its changing prospects, *Science of The Total Environment*, **824**, 153889.

Pirot E.M. and Edilbi A.N.F. (2023). Geochemical characteristics of bitumen seeps from the pila spi and bekhme formations:

insights from fourier transform infrared spectroscopy and trace metals, *Vibrational Spectroscopy*, **129**, 103607.

Pryshchepa O., Pomastowski P. and Buszewski B. (2020). Silver nanoparticles: Synthesis, investigation techniques, and properties, *Advances in Colloid and Interface Science*, **284**, 102246.

Ramaswamy N. and Mukerjee S. (2011). Influence of Inner- and Outer-Sphere Electron Transfer Mechanisms during Electrocatalysis of Oxygen Reduction in Alkaline Media, *The Journal of Physical Chemistry C*, **115**, 18015–18026.

Riaz M., Aamir M. and Shahzadi S. (2022). Structural, biological investigation of metal (Fe, Cu, Ag)-ceramic composites, *Journal of the Mechanical Behavior of Biomedical Materials*, **131**, 105265.

Salayova A., Bedlovičová Z. and Daneu N. (2021) Green Synthesis of Silver Nanoparticles with Antibacterial Activity Using Various Medicinal Plant Extracts: Morphology and Antibacterial Efficacy, *Nanomaterials* (Basel), **11**, 1005.

Saleh T.A., Mustaqeem M. and Khaled M. (2022). Water treatment technologies in removing heavy metal ions from wastewater: A review, Environmental Nanotechnology, *Monitoring & Management*, **17**, 100617.

Saravanan A., Senthil K.P. and Jeevanantham S. (2021). Effective water/wastewater treatment methodologies for toxic pollutants removal: Processes and applications towards sustainable development, *Chemosphere*, **280**, 130595.

Selmani A., Ulm L. and Kasemets K. (2020). Stability and toxicity of differently coated selenium nanoparticles under model environmental exposure settings, *Chemosphere*, **250**, 126265.

Sun Y., Xiong X. and He M. (2021). Roles of biochar-derived dissolved organic matter in soil amendment and environmental remediation: A critical review, *Chemical Engineering Journal*, **424**, 130387.

Tijani J.O., Fatoba O.O., Madzivire G. and Petrik L.F. (2014). A Review of Combined Advanced Oxidation Technologies for the Removal of Organic Pollutants from Water, *Water, Air and Soil Pollution: Focus*, **225**, 2102.

Uddin A., Siddique M.A.B. and Rahman F. (2020). Cocos nucifera Leaf Extract Mediated Green Synthesis of Silver Nanoparticles for Enhanced Antibacterial Activity, *Journal of Inorganic and Organometallic Polymers and Materials*, **30**, 3305–3316.

Weldegebrieal G.K. (2020). Synthesis method, antibacterial and photocatalytic activity of ZnO nanoparticles for azo dyes in wastewater treatment: *A review, Inorganic Chemistry Communications*, **120**, 108140. https://doi.org/10.1016/j.inoche.2020.108140

Woo G., Cho J. and Yeom H. (2023). Temperature-dependent phase transition in WS2 for reinforcing band-to-band tunneling and photoreactive random access memory application, *Small Science*, **4**, 2300202.

Zhao C., Zhou J. and Yan Y. (2021). Application of coagulation/flocculation in oily wastewater treatment: A review, *Science of The Total Environment*, **765**, 142795.